

PCCP

Accepted Manuscript



This is an *Accepted Manuscript*, which has been through the Royal Society of Chemistry peer review process and has been accepted for publication.

Accepted Manuscripts are published online shortly after acceptance, before technical editing, formatting and proof reading. Using this free service, authors can make their results available to the community, in citable form, before we publish the edited article. We will replace this *Accepted Manuscript* with the edited and formatted *Advance Article* as soon as it is available.

You can find more information about *Accepted Manuscripts* in the [Information for Authors](#).

Please note that technical editing may introduce minor changes to the text and/or graphics, which may alter content. The journal's standard [Terms & Conditions](#) and the [Ethical guidelines](#) still apply. In no event shall the Royal Society of Chemistry be held responsible for any errors or omissions in this *Accepted Manuscript* or any consequences arising from the use of any information it contains.



Journal Name

ARTICLE

In search of metal hydrides: An X-ray absorption and emission study of [NiFe] hydrogenase model complexes

Received 00th January 20xx,
Accepted 00th January 20xx

DOI: 10.1039/x0xx00000x

www.rsc.org/

Stefan Hugenbruch^a, Hannah S. Shafaat^{a,§}, Tobias Krämer^{a,†}, Mario Ulises Delgado-Jaime^{a,#}, Katharina Weber^a, Frank Neese^a, Wolfgang Lubitz^a and Serena DeBeer^{*a,b}

Metal hydrides are invoked as important intermediates in both chemical and biological H₂ production. In the [NiFe] hydrogenase enzymes, pulsed EPR and high-resolution crystallography have argued that the hydride interacts primarily at the Ni site. In contrast, in [NiFe] hydrogenase model complexes, it is observed that the bridging hydride interacts primarily with the Fe. Herein, we utilize a combination of Ni and Fe X-ray absorption (XAS) and emission (XES) spectroscopies to examine the contribution of the bridging hydride to the observed spectral features in [(dppe)Ni(μ-pdt)(μ-H)Fe(CO)₃]⁺. The corresponding data on (dppe)Ni(μ-pdt)Fe(CO)₃ are used as a reference for the changes that occur in the absence of a hydride bridge. For further interpretation of the observed spectral features, all experimental spectra were calculated using a density functional theory (DFT) approach, with excellent agreement between theory and experiment. It is found that the iron valence-to-core (VtC) XES spectra reveal clear signatures for the presence of a Fe-H interaction in the hydride bridged model complex. In contrast, the Ni VtC XES spectrum largely reflects changes in the local Ni geometry and shows little contribution from a Ni-H interaction. A stepwise theoretical analysis of the hydride contribution and the Ni site symmetry provides insights into the factors, which govern the different metal-hydride interactions in both the model complexes and the enzyme. Furthermore, these results establish the utility of two-color XES to reveal important insights into the electronic structure of various metal-hydride species.

1. Introduction

Hydrogenases catalyze the reversible oxidation of molecular hydrogen. These enzymes have attracted significant attention since they catalyze an environmentally benign reaction with very high efficiency.¹⁻⁴ Presently, the most efficient industrial catalysts for hydrogen conversion utilize precious metals, such as platinum.⁵ By contrast, nature uses first-row transition metals such as Fe and Ni to affect hydrogen conversion in the hydrogenase enzymes. The replacement of these expensive metal catalysts with inexpensive earth-abundant metals, such as those used in nature, is highly desirable. While [FeFe] hydrogenases have been subject of intense

studies for decades⁶⁻⁸, [NiFe] hydrogenases have attracted more attention within the last few years.⁹⁻¹⁷ The increased research interest in [NiFe] hydrogenases derives in part from the fact oxygen tolerant variants have been identified, which could have an enormous benefit for practical industrial applications.^{18, 19} Towards this end, there is much interest in understanding the detailed catalytic mechanism of the enzyme.

Scheme 1 shows the fragmentary proposed catalytic cycle for [Ni-Fe] hydrogenase, which has been derived from a combination of X-ray crystallography, electrochemistry, FTIR, and EPR spectroscopic studies.²⁰⁻²¹ The paramagnetic Ni-B and Ni-C states have been intensely studied by electron paramagnetic resonance (EPR) methods, which first established the presence of a hydride bridge in Ni-C.²² Very recently, Ogata et al., reported a subatomic resolution crystal structure of Ni-R, which verified the presence of the bridging hydride, with Ni-H and Fe-H distances of 1.58 and 1.78 Å, respectively, providing support for a low-spin Ni site with a dominantly Ni bound hydride species in the protein.^{23, 24} This feature is thought to play a key role in the high catalytic rates of the enzyme. However, even in a 0.89 Å crystal structure, uncertainties of about 0.2 Å for the M-H bonds remain.

^a Max-Planck-Institute for Chemical Energy Conversion, Stiftstr. 34 – 36, Mülheim a. d. Ruhr, D-45470, Germany

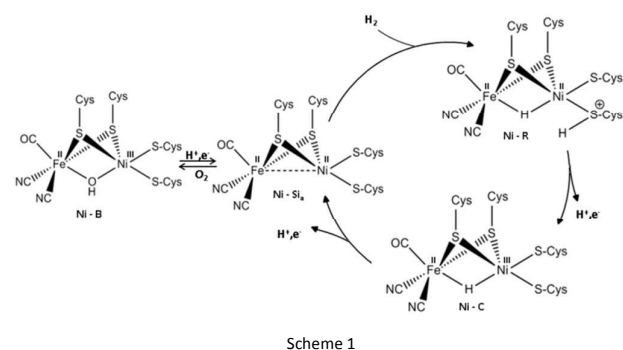
^b Cornell University, Department of Chemistry and Chemical Biology, Ithaca, New York, 14853, United States

[§] The Ohio State University, Department of Chemistry and Biochemistry, 100 West 18th Avenue, Columbus, OH 43210-1173, USA

[†] Heriot-Watt University, Institute of Chemical Sciences, Edinburgh EH14 4AS, UK

[#] Inorganic Chemistry and Catalysis Group, Debye Institute for Nanomaterials Science, Utrecht University, Universiteitsweg 99, Utrecht 3584 CG, the Netherlands

Electronic Supplementary Information (ESI) available: [xyz coordinates of calculated structures]. See DOI: 10.1039/x0xx00000x



Small molecule model complexes have been developed, which are capable of mimicking various aspects of the protein active site – including the short metal-metal distances²⁵⁻²⁸, the possible protonation of a terminal sulfur²⁹ and the reduction of substrates by hydride transfer or electron transfer.³⁰ While some of these model complexes mimic the Ni-R and Ni-Si₃ states partially, none of the models show catalytic activity that is comparable to that of the enzyme active site.

In contrast to the enzyme, all crystallographically characterized NiFe model complexes, where a metal-hydride bond has been identified, have asymmetric metal hydride distances with the Fe-H bond being shorter than the Ni-H bond (Table 1). The extreme case of this asymmetry is found in a NiFe model recently reported by Ogo and coworkers in which the Fe-H is 1.57 Å and the Ni-H is 2.16 Å. This finding was utilized by these authors to argue that the Fe-H interaction may be more relevant to intermediates in the enzymatic catalytic cycle than a Ni-H interaction.³⁰ In contrast in the (dppe)Ni(μ-pdt)(μ-H)Fe(CO)₃ complex (**2**) first reported by Rauchfuss and coworkers, the Ni-H and Fe-H distances are much more similar (Table 1); however the hydride coordination still appears to favor the iron. This is also the case in all subsequently reported variants from the Rauchfuss laboratories.²⁶⁻²⁸

One must caution, however, that the errors in metal-hydride bond length determination by crystallographic methods are very high, with 3σ values in Table 1 ranging from 0.06-0.21 Å. While pulsed EPR methods can undoubtedly provide complementary insights into M-H interactions³¹, the requirement for paramagnetic species is somewhat limiting. Hence, alternative methods for the experimental evaluation of M-H interactions are highly desirable. Another interesting difference between the model complexes and the protein active site is that in the hydride bound models the Ni has a local square planar symmetry with the NiL₄ unit (where L corresponds to the non-hydride ligands, thus excluding any M-H or M-M contributions).

Table 1 Crystallographic metal-hydride distances for the enzyme and model complexes. The values in parentheses are the reported sigma values.

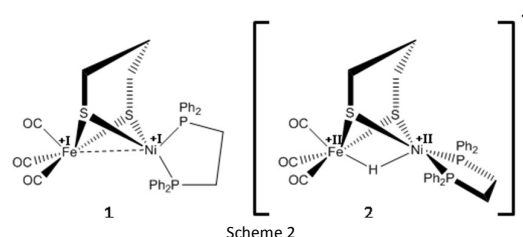
	Ni-H [Å]	Fe-H [Å]
[NiFe]hydrogenase Ni-R ²³	1.58(7)	1.78(7)
[(dppe)Ni(μ-pdt)(μ-H)Fe(CO) ₃]BF ₄ (2) ²⁶	1.64(5)	1.46(7)
[(dppe)Ni(μ-pdt)(μ-H)Fe(CO) ₂ (PR ₃)]BF ₄ ²⁷	1.89(3)	1.49(3)
[(dcpe)Ni(μ-pdt)(μ-H)Fe(CO) ₃]BF ₄ ²⁸	1.90(2)	1.53(2)
[(dppe)Ni(μ-edt)(μ-H)Fe(CO) ₃]BF ₄ ²⁸	1.84(3)	1.58(4)
[(X')Ni(μ-H)Fe(MeCN){P(OEt) ₃ } ₃]BPh ₄ ³⁰	2.16(4)	1.57(5)

Even in cases where the Ni is initially in a locally pseudo-tetrahedral (*T_d*) geometry (e.g. in the unprotonated precursors, such as **1**), a change to pseudo-*D_{4h}* symmetry occurs upon protonation.²⁶⁻³⁰ This distortion leads to a dramatic change in the ligand field at the Ni center. As discussed by Hyunh et al.,³² this can result in altered reactivity at the neighboring Fe site, with the Fe-H bond being stronger than the Ni-H bond. This is in stark contrast to the enzyme system, where it is generally agreed that a non-planar NiL₄ geometry is maintained throughout the catalytic cycle.² Presumably this allows for the Ni-H interaction to be stronger than in the model complexes. In this context, experimental tools, which allow for both the Ni-H and Fe-H interactions to be selectively probed are highly desirable.

In this work, a combined spectroscopic and computational approach is utilized to assess 1) the presence of metal-hydride interactions and 2) the influence of Ni site geometry on the metal-hydride bond strength. Detailed experimental and computational studies have been performed on the two NiFe model complexes, (dppe)Ni(μ-pdt)Fe(CO)₃ (**1**)²⁵ and [(dppe)Ni(μ-pdt)(μ-H)Fe(CO)₃]⁺ (**2**)²⁶, shown in Scheme 2.

Specifically, X-ray absorption spectroscopy (XAS) and X-ray emission spectroscopy (XES), have been utilized due to their ability to detect changes in local site symmetry and coordination environment in an element selective fashion. XAS detects the excitation of a 1s core electron (K-edge) to empty orbitals in the valence shell and beyond. The transitions to the valence shell (1s-3d) and to the unoccupied 4p orbitals shed light on the local geometry of the metal center as well as on its oxidation state. An XES spectrum arises, when a 2p (Kα), 3p (Kβ), or valence electron relaxes (VtC) to fill a 1s core hole on a transition metal absorber. The Kβ mainline region can be used as a measure for spin states, with additional modulations due to covalency.³³ VtC XES has been shown to be an excellent tool to identify light atom bridging ligands.³⁴⁻³⁶ Reports have been published that aimed at the identification of an iron hydride in [FeFe] hydrogenase.³⁷ Hence, this method is ideally suited to separately examine the possible Ni-H and Fe-H bonds.

The experimental results are correlated to density functional theory calculations (DFT) of both the XAS and XES spectra. The good agreement between theory and experiment allows us to systematically investigate the effects of both, local site geometry and protonation. Additionally, we examine the factors which govern a preferential hydride interaction with the Fe or Ni centers. Finally, the ability to use VtC XES as a quantitative probe of M-H bond lengths is explored. These results should have broad applicability to all areas of metal-hydride research.



2. Materials and Methods

2.1. Sample Preparation

Compounds **1** (dppe)Ni(μ -pdt)Fe(CO)₃ and **2** (dppe)Ni(μ -pdt)(μ -H)Fe(CO)₃ were synthesized according to reported procedures^{25,26}. For XAS measurements, powder samples of **1** and **2** were ground, diluted with solid BN, transferred to 1mm Al sample holders, sealed with 38 μ m Kapton tape and immediately frozen in liquid N₂. For XES measurements, powder samples of **1** and **2** were ground, transferred to 1mm Al sample holders, sealed with 38 μ m Kapton tape and immediately frozen in liquid N₂.

2.2. X-ray Spectroscopy

XAS data were collected at SSRL beam line 7-3 (3 GeV, 350 mA). A liquid N₂ cooled Si(220) monochromator was used for energy selection. The incident energy was calibrated with references to the first inflection points of Fe and Ni foils at 7111.2 eV and 8331.7 eV, respectively. Focusing mirrors were used to achieve a 1 x 10 mm² beam spot at the sample, providing $\sim 10^{12}$ photons/s. If necessary, to prevent beam damage or detector saturation, Al filters were inserted before the sample to attenuate the incident beam. Total fluorescence data were collected using a PIPS detector. Two different XAS scan regions were utilized in each case. For Fe XAS data, in the region from 6785 to 7085 eV steps, from 7085 to 7150 0.15 eV steps and from 7150 to 7990 an increasing step size of 0.9 – 6 eV was used, respectively. For Ni, in the region from 8010 to 8310 5 eV steps, from 8310 to 8370 0.15 eV steps and from 8370 to 8900 a step size of 3.5 eV was used.

For both compounds **1** and **2** the average of four scans was utilized to generate the spectra analyzed above. After a second order polynomial background subtraction, the averages were normalized to an intensity of 1 between 7800 eV - 7990 eV for Fe and between 8700 eV – 8900 eV, respectively.

Fe and Ni XES spectra were collected at SSRL beam line 6-2 (3 GeV, 350 mA). The incident beam energy was set to 7800 eV in the case of Fe, and 9320 eV in the case of Ni using a Si(111) liquid-nitrogen-cooled monochromator. Aluminum filters were inserted before the sample to attenuate the incident beam. Additional filters were used for the mainline region (to prevent detector saturation), compared to the VtC region where the number of filters was optimized to improve signal-to-noise ratio and to minimize beam damage. For energy resolution of the XES spectra, a crystal array spectrometer was utilized, employing five spherically bent Ge(620) (with 100 mm diameter and 1 m radius of curvature) for Fe, and three spherically bent Si(551) crystals (with 100 mm diameter and 1 m radius of curvature) for Ni. Samples were maintained at ~ 10 K in an Oxford CF1208 continuous flow liquid helium cryostat and were positioned at 45° with respect to the incident beam. A He filled path was used between the sample and spectrometer to reduce signal attenuation and emitted X-rays were detected using an energy resolving SDD (Si drift detector) with a 3 mm vertical slit.

Two different scan regions were utilized for data collection. The first region was through the intense K β mainline and the second through the less intense VtC region. In the case of Fe, the K $\beta_{1,3}$ scans were collected in the energy region of 7020 to 7085 eV with steps of 0.2 eV, whereas the VtC scans span the energy range of 7080 to 7130 eV with steps of 0.15 eV. In the case of Ni, the K $\beta_{1,3}$ scans were collected over the energy range of 8235 to 8290 eV with steps of 0.25 eV and the VtC scans from 8285 to 8350 eV, also with steps of 0.25 eV. In each case, an average of the scans was taken for each region and the resulting averages merged to form the Fe and Ni VtC XES spectra.

The Fe K β XES data were calibrated using the reference spectra for Fe₂O₃. The Ni K β XES data were calibrated by Gaussian fitting the elastic scatter peaks at 24 energy points in the range 8240 – 8350 eV. These fits were used to obtain the linear fit, which was used for the calibrated energy scale of the XES data.

For both compounds **1** and **2**, the average of two scans for the mainline region and the average of ten scans for the VtC region were utilized to generate the spectra analyzed above. The merged spectra were fit using a reported model³⁸ and the methodology for fitting in BlueprintXAS.^{39,40} From the resulting fits all lower energy contributions to the VtC region (i.e. tails from the K β region) were subtracted and the isolated VtC area was normalized to 1.

2.3. Computations

All calculations were performed using the ORCA quantum chemistry package (version 3.0).⁴¹ Initial geometries for **1** and **2** were obtained from X-ray crystal structures.^{25,26} Unconstrained geometry optimizations were carried out with the BP86 functional^{42,43} in conjunction with the RI-J approximation⁴⁴⁻⁴⁷ and the def2-TZVP basis set on all atoms, combined with the matching def2-TZVP/J auxiliary basis set.⁴⁸⁻⁵¹ For the hypothetical models **1*** and **2*** the hydrogens were optimized, while the remaining atoms were kept frozen. For XAS and XES calculations the BP86 functional^{42,43} was used in conjunction with the def2-TZVP(-f) basis set and the def2-TZV/J auxiliary basis set⁴⁸⁻⁵¹ on all atoms except Fe, for which the expanded CP(PPP) basis set was used⁵². The radial integration accuracy on Fe and Ni was increased to 7 (SpecialGridIntAcc 7). Complexes were embedded in a conductor-like screening model (COSMO) with an infinite dielectric.⁵³ XAS spectra were subsequently derived via time-dependent DFT (TD-DFT) calculations^{54,55}, while the XES spectra were calculated within the framework of a one-electron approach⁵⁶, both using a single point protocol on optimized complex geometries. MOAnalyzer was used for population analysis.⁵⁷ Calculated VtC XES spectra were renormalized to an area of 1 for direct comparison to the experimental data.

3. Results

Table 2 provides important bond metrical parameters for **1** and **2** both from the X-ray structure^{25,26} and the DFT-optimized

structure.¹⁴ The Fe environment in **1** is comprised of 3 CO ligands and 2 Fe-S (dithiolate) bonds. Upon protonation to form **2** the local geometry at the Fe site changes from close to square-pyramidal to pseudo-octahedral due to the presence of an Fe-H bond. While the Fe coordination environment remains almost unchanged upon protonation, the local geometry at the Ni site proceeds from nearly T_d to nearly D_{4h} within the NiS_2P_2 unit.

For all spectral calculations, geometry optimized structures were utilized, as discussed in section 2.3. Prior to comparison of the calculated and experimental spectra, a comparison of the crystal structure and the optimized structure is revealing. All bond lengths in the first coordination sphere of the optimized structure of **1** are within 0.03 Å of the crystal structure. Similarly good agreement for all distances are found for the protonated complex **2**, with the exception of the M-H bond lengths, where the Fe-H and Ni-H bonds are 0.16 Å and 0.11 Å longer, respectively, than in the corresponding crystal structure. These differences underscore the challenges in the accurate determination of M-H distances. A quantitative approach to determine M-H bond lengths via VtC XES is discussed in section 4.2.

3.1. XAS

3.1.1. Iron XAS Figure 1a shows the normalized Fe K-edge XAS spectra of **1** and **2**. Upon protonation, the spectral changes are consistent with an increase of Z_{eff} in Fe. Namely the pre-edge transition (Figure 1b), in the 7110-7116 eV region, shifts from peak maxima of 7112 and 7114.5 eV in **1** to maxima of 7113 eV and 7115.5 eV in **2**. Based on previous investigations on Fe complexes, the low energy pre-edge peak should be attributed to a 1s to 3d transition, while the higher energy feature likely corresponds to transitions to unoccupied carbonyl π^* based orbitals.⁵⁸⁻⁶⁰ The ~0.5-1 eV shift in both the pre-edge and edge features, is consistent with an increase in oxidation state from Fe(I) to Fe(II) upon protonation.

Table 2 Atomic distances (in Å) and dihedral angle between Ni-S₂ and Ni-P₂ planes of **1** and **2** from XRD and DFT optimized structures.

	1 (XRD)	1 (DFT)	2 (XRD)	2 (DFT)
Fe-Ni	2.47	2.45	2.61	2.59
Fe-H	-	-	1.46	1.62
Ni-H	-	-	1.64	1.75
Fe-C1	1.80	1.77	1.79	1.77
Fe-C2	1.80	1.77	1.80	1.78
Fe-C3	1.80	1.78	1.80	1.79
Fe-S1	2.28	2.29	2.32	2.35
Fe-S2	2.28	2.31	2.32	2.36
Ni-S1	2.23	2.24	2.21	2.22
Ni-S2	2.28	2.27	2.22	2.22
Ni-P1	2.15	2.12	2.16	2.15
Ni-P2	2.16	2.13	2.17	2.16
Dihedral Ni-P-S	84.9	84.0°	4.9°	0.2°

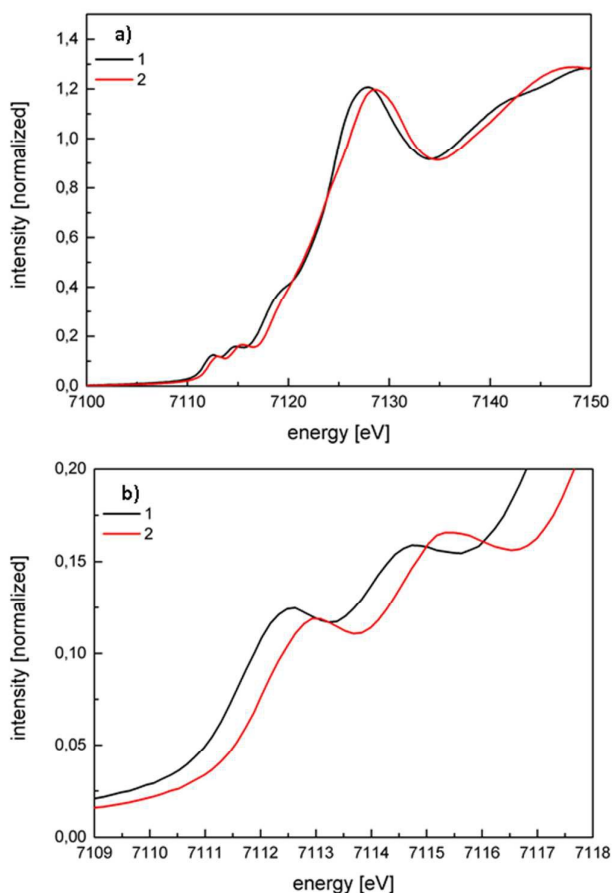


Figure 1 a) Fe K-edge XAS spectra of **1** and **2**. b) Expanded pre-edge region of **1** and **2**. The shift in energy is consistent with an increase in oxidation state from +I to +II.

3.1.2. Ni XAS The Ni K-edge XAS spectra (Figure 2a) show similar changes when comparing **1** to **2**. In addition to the pre-edge, located at 8331 eV, features are observed in the rising edge region of **1**. The spectral features in the rising edge are most likely attributed to 1s-4p transitions, whereas, similar to Fe case, the lowest energy peak corresponds to a 1s-3d transition. This pre-edge feature is no longer present in **2** (Figure 2b), but instead a spectral feature at 8334 eV appears.

Based on previous studies on Ni complexes⁶¹, the $4p_z$ orbital is most likely shifted to lower energies in **2**, due to the local D_{4h} symmetry within the NiS_2P_2 unit. Hence, the 1s to $4p_z$ transition likely obscures the weak quadrupole allowed 1s-3d transition in **2**. The coupled geometric and electronic changes, which occur at the Ni center on going from **1** to **2**, complicate a quantitative assignment of the spectroscopic oxidation state of the Ni center in **2**. While it is generally assumed that the Ni oxidation state increases from Ni(I) to Ni(II) upon conversion to **2**, the experimental assignment based on the Ni K-edges depends strongly on where one chooses to measure the rising edge. This picture is further complicated by the fact that shakedown transitions, which depend strongly on metal ligand covalency, are superimposed on the rising edge. In this regard, **2** has shorter, more covalent Ni-S bonds than **1**. Although this increase in covalency would lead to destabilized $4p_x$ and $4p_y$

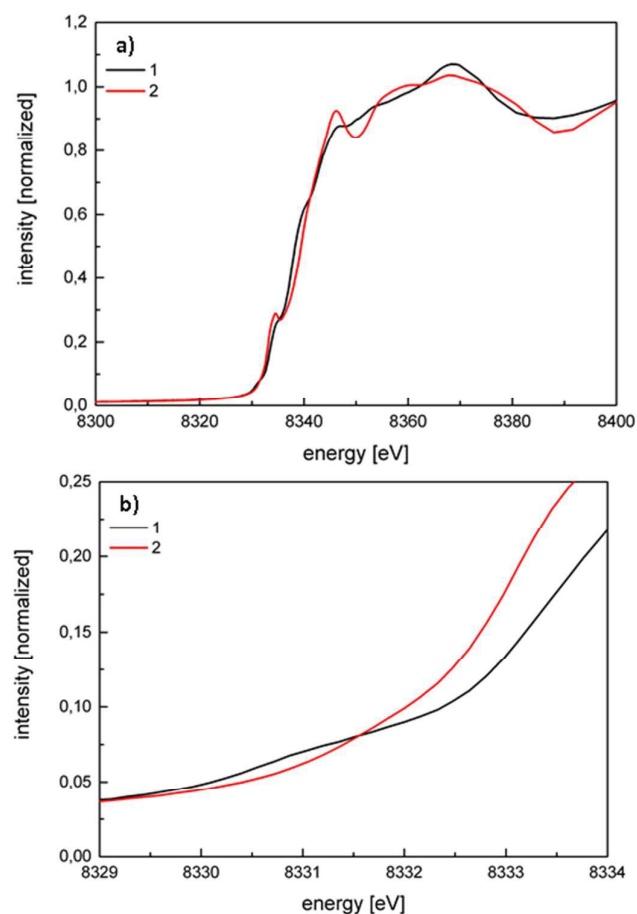


Figure 2 a) Ni K-edge XAS spectra of **1** and **2**. b) Expanded pre-edge region of **1** and **2**. The 1s-3d transition, which is observable in **1** is shifted to higher energies in **2**. In addition to this the 1s-4pz transition is stabilized in the D_{4h} geometry, hence also contributing intensity to the pre-edge region.

orbitals, the ligand-to-metal charge transfer shakedown transition will shift to lower energies with increased covalency.³³ Due to this combination of factors, a more quantitative assessment of Ni K-edge data are, at present, not possible on the basis of experimental spectra and will be done in section 3.3..

3.2. XES

3.2.1. Iron XES Figure 3 shows the normalized experimental Fe K β XES spectra of **1** and **2**. While the K β mainlines of the two model complexes overlap (Figure 3a), the VtC region (Figure 3b) shows an increase in intensity at 7107 eV and a loss at \sim 7110 eV. According to previous studies, the mainline is affected by oxidation state as well as by covalency.³³ Hence, although the increase in oxidation state would lead to a K $\beta_{1,3}$ that is energetically slightly higher in energy, the increase in covalency counteracts this effect. In the VtC region, the spectral features between 7100 eV and 7105 eV have previously been shown to be fingerprints of CO ligands.^{38,60} As the primary changes which occur at the Fe site are the formation of the Fe-H bond and the elongation of the Ni-Fe bond, the spectral differences occurring at 7107 eV and \sim 7110 eV can most likely be attributed to

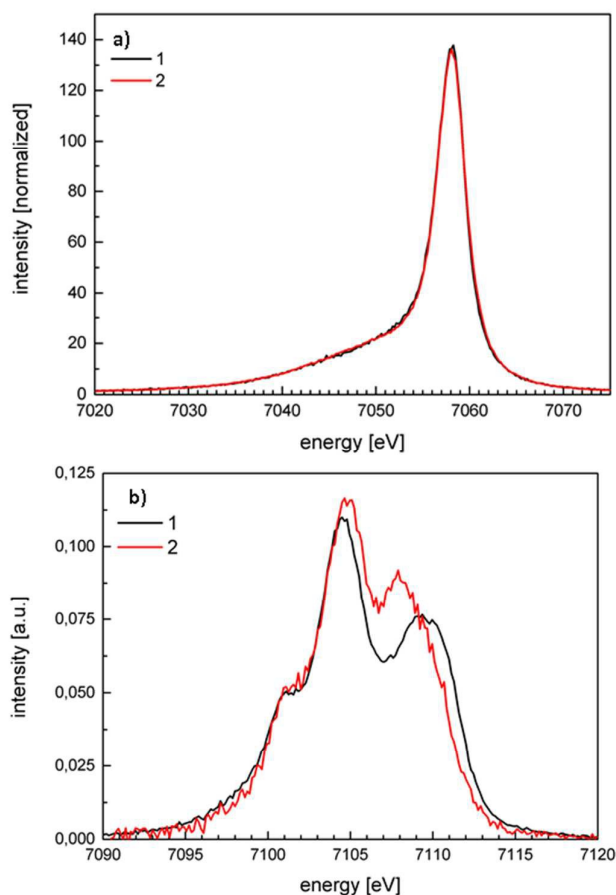


Figure 3 a) Normalized Fe K β mainline spectra of **1** and **2**. Due to opposing effects of oxidation state and covalency changes, the mainlines appear unchanged upon protonation. b) Mainline-subtracted and renormalized Fe VtC spectra of **1** and **2**. The increase in intensity at 7107 eV can be attributed to the formed Fe-H bond.

the protonation of the iron and the associated elongation of the metal-metal bond. It is assumed that the higher energy feature would derive from filled metal-based orbitals, while the 7107 eV feature could derive from a hydride based molecular orbital. These empirical assumptions are explored more quantitatively in the computational section, *vide infra*.

3.2.2. Ni XES As was the case for the Fe K β XES mainline spectra, effectively no changes are observed in the Ni K β XES mainline spectra of **1** and **2** (Figure 4a). We again attribute this to canceling contributions of covalency and spin state, which in this case, also inhibited the interpretation of the edge data.

However, the changes in the VtC spectra on going from **1** to **2** are more pronounced than the changes that occur in the mainlines (Figure 4b). Rather than the prominent CO fingerprints seen at iron, there is now a combined signature from the dppe and dithiolate ligands present on the low energy side of this spectral region. Similar to the Fe spectra, a gain in intensity can be observed upon protonation, in this case at \sim 8329 eV. In addition, the high energy feature at \sim 8331 eV vanishes. As the Ni center undergoes a local change in geometry, in addition to the Ni-Fe bond elongation and

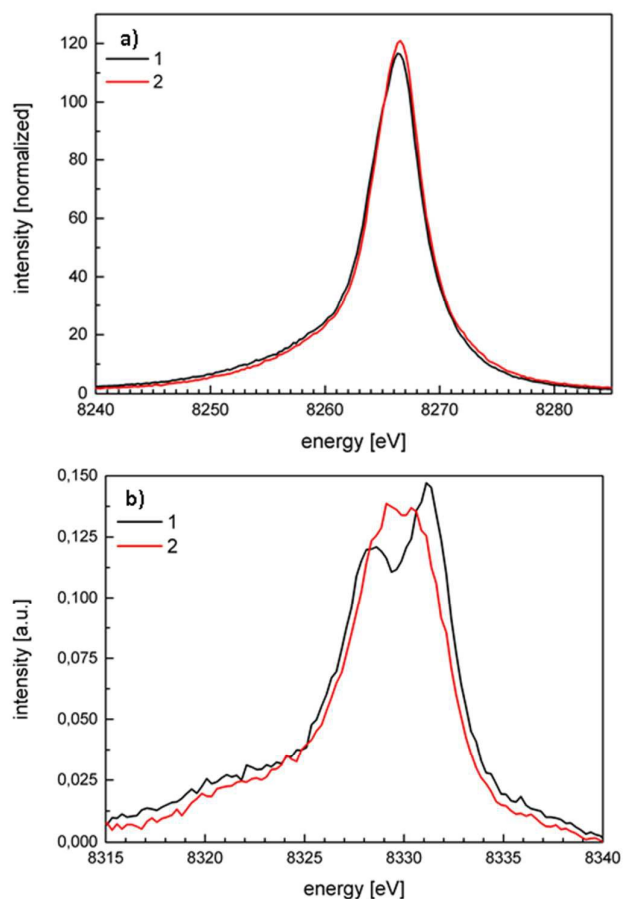


Figure 4 a) Normalized Ni K β XES mainline spectra of **1** and **2**. Due to opposing effects of oxidation state and covalency, the mainlines do not change upon protonation. b) Mainline subtracted and renormalized Ni VtC spectra of **1** and **2**. The increase in intensity at 8329 eV can be attributed to either the protonation, the geometry distortion or a combination of both.

protonation, the origin of the spectral changes may be based on any one or a combination of these effects. Thus, the structural origin of the observed changes is quantitatively investigated through computational studies in the next section.

3.3. Computations

The calculated pre-edge transitions of the Fe K-edge are displayed in comparison with the experimental data in Figure 5a. The calculations reasonably reproduce the 1 eV shift of the 1s-3d transition to higher energies upon protonation. However, the higher energy pre-edge features are not well modeled. Based on previous studies, we surmise that these features likely arise from ligand-to-metal charge transfer features, which are generally not well-modeled within a TD-DFT approach.^{62,63} Nonetheless the good agreement for the lowest energy 1s to 3d features indicates that the calculated electronic structures are consistent with the experiment.

For the calculated Ni K- pre-edge spectra, the agreement is very good, with a pre-edge feature present for **1** and absent for **2**. The

differences in these spectra can be readily understood by simple symmetry considerations. As **2** has a locally square-planar geometry within the NiS₂P₂ unit, mixing of the empty $d_{x^2-y^2}$ orbital and the p orbitals is forbidden by symmetry. Furthermore, one may expect weak quadrupole allowed transitions. However, the strong in plane ligand donation also increases the energy of the $d_{x^2-y^2}$ orbital by ~ 1 eV, thus burying the corresponding 1s \rightarrow 3 $d_{x^2-y^2}$ spectral feature in the rising edge. The presence of any pre-edge feature in complex **2** is further masked by the fact that the 4p_z orbitals stabilized in a square-planar geometry. This results in a lower energy rising edge feature that should be attributed to the 1s \rightarrow 4p_z transition and would fully obscure any observable pre-edge intensity. This simple picture is nicely confirmed by the calculations which show an energy shift of the $d_{x^2-y^2}$ orbital from ~ 8331.1 eV to ~ 8332 eV. The calculations also predict weak quadrupole allowed intensity at 8332 eV for **2** compared to the dipole allowed transition at 8331.1 eV for **1**.

The calculated iron and nickel VtC XES spectra of **1** and **2** (Figure 6) match the experimentally observed trends very well. While the feature at 7107 eV in the calculated Fe XES spectrum of **2**

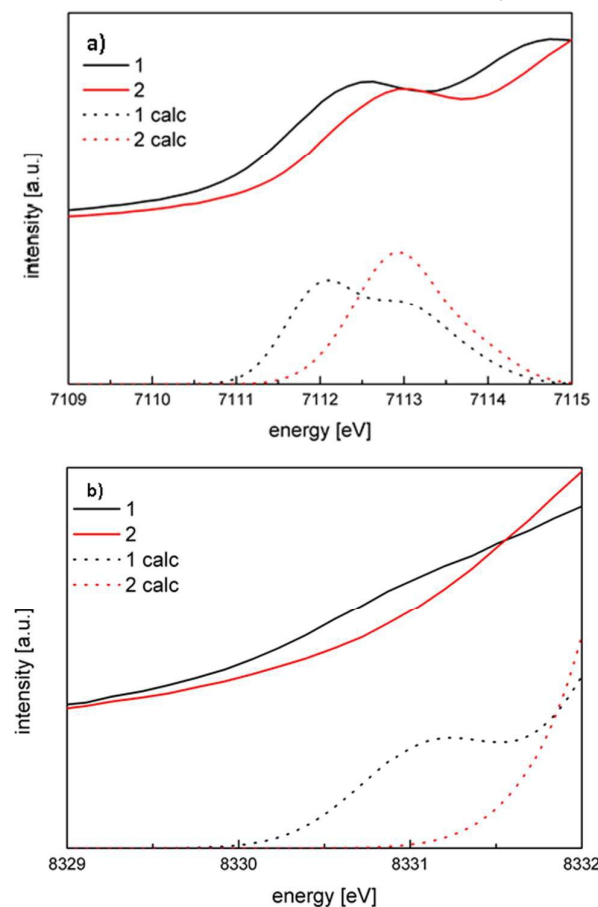


Figure 5 Comparison of the experimental (solid) and calculated (dotted) a) Fe XAS spectra and b) Ni XAS spectra of **1** and **2**. Differences in a) can be attributed to charge transfer transitions, as TD-DFT is limited in reproducing these. The difference in intensity in b), may be attributed to the intense tail of the edge transitions, which is present only in the experimental data. For the calculated spectra a shift of 181.5 eV (in the case of Fe) and 212.5 eV (in the case of Ni) as well as a broadening of 1 eV was applied.

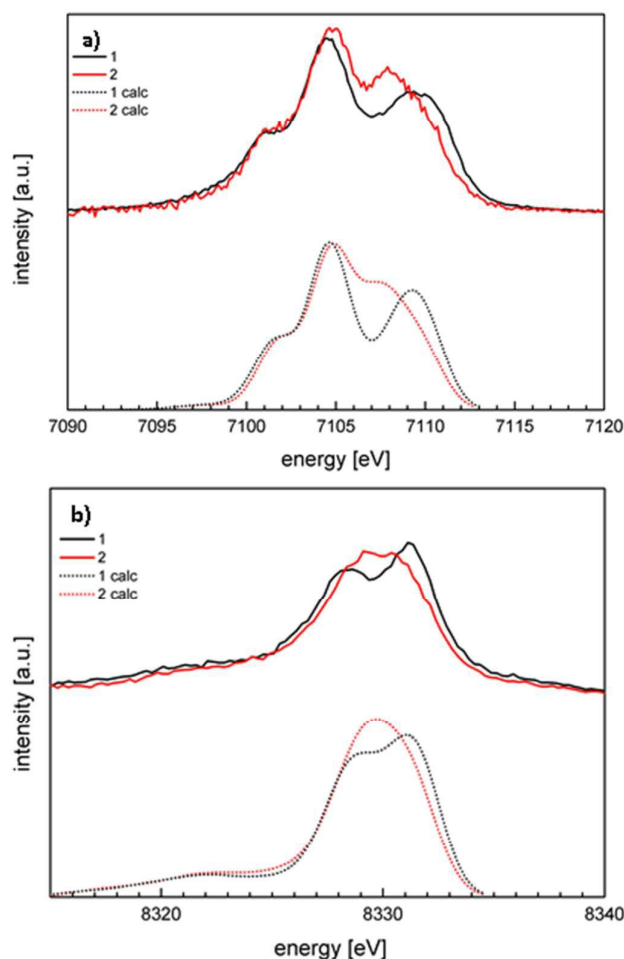


Figure 6 Comparison of the experimental (solid) and calculated (dotted) a) Fe VtC XES spectra and b) Ni VtC XES spectra of **1** and **2**. An energy shift of 182 eV (Fe) and 215.5 eV (Ni), respectively has been applied. These spectra were generated from a calculated sticks spectrum with a broadening of 2.5 eV.

(Figure 6a) can be attributed to the Fe-H interaction, the increase in intensity at 8329 eV in the calculated Ni XES spectrum (Figure 6b) corresponds to a molecular orbital with only a very small fraction in Ni-H character. The residual intensity gain upon protonation will be investigated in more detail in the next section.

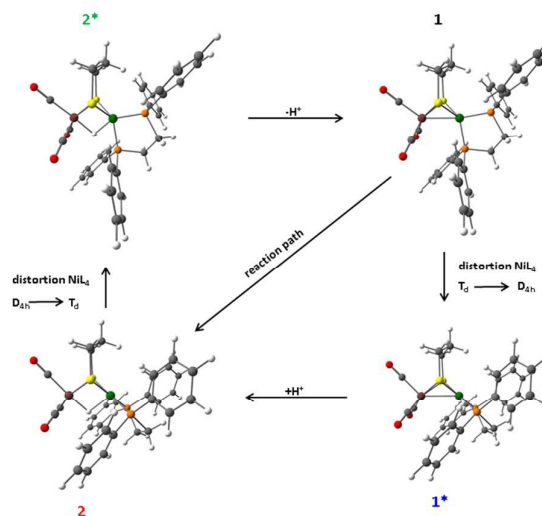
4. Discussion

4.1. Computational Investigation of Symmetry vs. Protonation on Observed Spectral Features

In order to systematically understand the origin of the XAS and XES spectral changes on going from **1** to **2**, spectra for hypothetical structures **1*** and **2*** were calculated (Scheme 3). In structure **1***, the geometry at the Ni center was distorted from pseudo-tetrahedral to pseudo-square-planar (as occurs in **2**), however the proton was not yet added to the bridge. Thus, the hypothetical model **1***, allows for an independent evaluation of the contribution of the geometry change at the Ni to the observed spectra. In an

analogous fashion, in hypothetical model **2***, the Ni was forced to stay in its initial T_d geometry (as observed in **1**), while also adding a proton to the bridge. This allowed for a distinct evaluation of the contribution of the proton, at either tetrahedral or square-planar geometry. Models **1** and **2** were fully optimized, whereas model **1*** was obtained from optimized **2** by removal of the bridging proton. Manual addition of a proton to the bridging position in **1** and subsequent geometry optimization of its position whilst keeping all remaining atoms fixed at their equilibrium positions yielded structure **2***. Interestingly, in **2***, the Ni-H and Fe-H distances go from being asymmetric towards Fe in **2** (with a Fe-H distance of 1.62 Å and a Ni-H distance of 1.74 Å) to asymmetric towards Ni in **2*** (with a Fe-H distance of 1.64 Å and a Ni-H distance of 1.59 Å). Whether or not these metal hydride distances correspond to formal M-H bonds is discussed in more detail below.

The calculated Fe and Ni K-edge XAS pre-edge spectra of **1**, **1***, **2** and **2*** are shown in Figure 7a and 7b, respectively. Ongoing from structure **1** to **1*** the calculated 1s to 3d transition at the Fe K-edge is essentially unchanged (Figure 7a), consistent with the fact that no changes have occurred in the direct Fe coordination environment. Upon protonation to form **2**, the oxidation state of the Fe center is increased from Fe(I) to Fe(II). This results in a shift of the pre-edge to higher energies, which is reflected in the calculated spectra (and also consistent with the observed experimental changes between **1** and **2**). Ongoing to structure **2***, the calculated Fe K- pre-edge is lower in both energy and intensity, indicating that although the Fe is still formally Fe(II), the electronic structure at the Fe site has been modulated by the distortion at the Ni. This may derive from a difference in the Ni-Fe interaction and/or the elongation of the Fe-H bond. This point is addressed in further detail below, via analysis of the localized orbitals.



Scheme 3

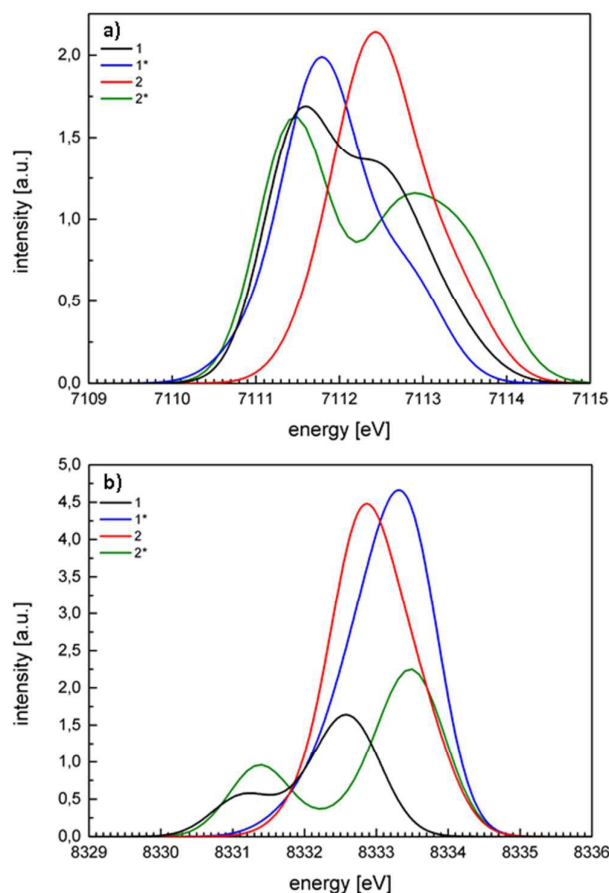


Figure 7a) Calculated Fe XAS spectra of **1**, **1***, **2** and **2*** (shifted by 181.5 eV; 1 eV broadening applied). b) Calculated Ni XAS spectra of **1**, **1***, **2** and **2*** (shifted by 212.5 eV; 1 eV broadening applied).

It is well established that in centrosymmetric symmetries p-d-mixing does not occur⁵⁸. This effect can be observed in the Ni XAS pre-edge calculations of this cycle (Figure 7b). The two pseudotetrahedral structures (**1**, **2***) both have a visible pre-edge (at ~8331 eV), while the pseudo-square-planar ligand environments (**1***, **2**) show no observable pre-edge intensity, but are instead dominated by an intense 1s to 4p_z transition (at ~8333 eV), which overlap the weak 1s to 3d transitions (at ~8332 eV).

The Fe and Ni VtC regions of the calculated XES spectra are depicted in Figure 8a and 8b, respectively. The Fe VtC spectra (Figure 8a) remain similar when going from **1** to the hypothetical model **1***. The loss in intensity on the high-energy side is due to a decrease in the total metal-metal bonding interaction from a Mayer bond order of 0.45 to 0.29. In **1**, the HOMO-1 to HOMO-6 all have between 30% and 50% combined Fe and Ni d-character, while in **1*** these orbitals do not exceed 20% – 35% combined Fe and Ni d-character. The decrease in metal character can be attributed to the geometric differences, which disfavor metal-metal bonding. Upon protonation to **2** an increase in intensity at ~7107 eV is observed in the calculated spectrum. This increase in intensity can be attributed to the addition of the proton and the resulting iron-hydride bond. Ongoing to the hypothetical model **2***, the feature at ~7107 eV is

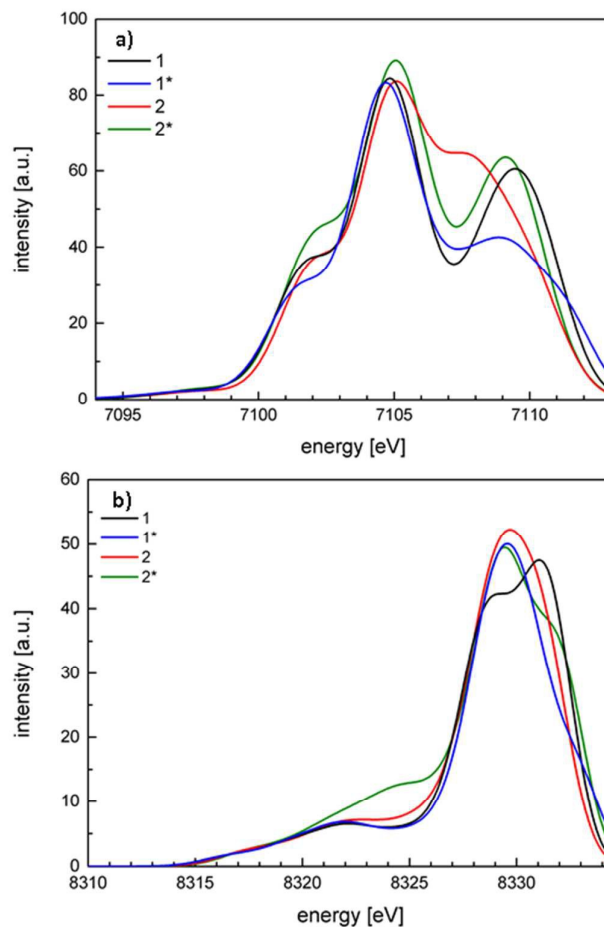


Figure 8 a) Calculated Fe spectra XES (shifted by 182 eV; 2.5 eV broadening applied) and b) calculated Ni XES spectra (shifted by 215.5 eV; 2.5 eV broadening applied) of **1**, **1***, **2** and **2***.

still present, but decreases in intensity compared to model **2**. This indicates a decreased Fe-H contribution when the Ni is in a tetrahedral geometry. In addition, the Fe-H distance elongates going from **2** to **2*** by 0.02 Å. Hence, the overlap between the atomic orbitals decreases, which also results in a loss of intensity of this feature.

In the Ni VtC XES spectra (Figure 8b) one observes an increase in the intensity at ~8329.5 eV on going from **1** to **1***. Since the only difference between these two structures is the geometry around the Ni center, this must be the origin of the intensity increase, which can be explained by the change in the ligand field upon distortion. This change is reflected by an increase of 5% p-character (from the S- and P- 3p levels) of the corresponding orbitals (going from ~55% to ~60%). Upon protonation to **2** there is almost no change in the Ni VtC spectra. This indicates little or no Ni-hydride contribution to the spectrum. In contrast, for model **2*** (where the Ni is retained in a tetrahedral ligand field, as in structure **1**), there are notable intensity increases at ~8324.5 and 8329.5 eV (relative to **1**), which in this case may only reasonably be attributed to the presence of a Ni-H bond.

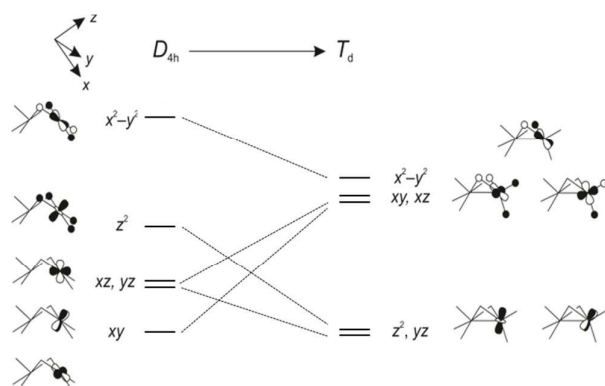


Figure 9 Orbital correlation diagram of Ni d orbitals at D_{4h} and T_d geometry. The energy level ordering of the d-orbitals was based on visualization of canonical orbitals from the ground state DFT calculations of **1** and **1***. For clarity, idealized d-orbitals are depicted.

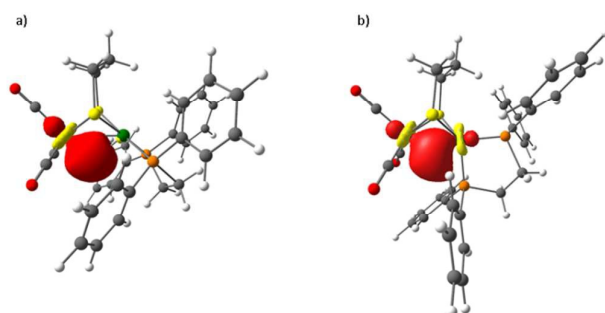
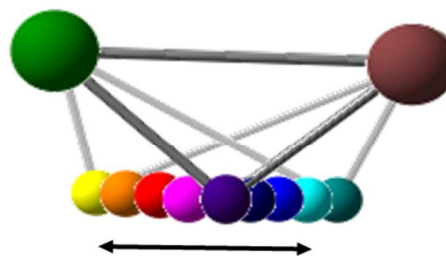


Figure 10 Localized M-H orbitals of a) **2** and b) **2***.

The spectral changes described above all suggest a single Fe-H bond in **2** (and no Ni-H bond), which is in agreement with previous published data^{26,32}, while the hypothetical model **2*** shows a clear indication of a Fe-H-Ni hydride bridge (i.e. both Ni-H and Fe-H bonding interactions are present). A schematic orbital correlation diagram for a D_{4h} to T_d local distortion at Ni (Figure 9) provides a means to readily visualize the origin of the observed electronic structural changes. Namely the ability of **2*** to form a bridging hydride may be attributed to stabilization of the Ni $d_{x^2-y^2}$ orbital in tetrahedral geometry, which allows for a sigma interaction between the Ni and the hydride.⁵⁹ Visualization of the localized orbitals provides further support for this bonding description (Figure 10).

4.2. Asymmetry in the Hydride Bridge

The analysis in the preceding section, suggests that a hydride can only interact with both the Ni and the Fe, when the Ni can adopt a favorable local site geometry. However, clear discrepancies remain between the crystallographic M-H distances for complex **2** and those obtained from the DFT geometry optimizations. Namely, the DFT calculations predict Fe-H and Ni-H bonds that are 0.16 Å and 0.10 Å longer than the crystal structure. While the above analysis certainly suggests that VtC XES should be able to determine if a M-H interaction is present, it does not assess the contribution of the M-H distance. However, as previous studies have shown that the VtC intensity is sensitive to M-L bond distances,^{54, 65, 66} this information



Scheme 4

should also be accessible from a quantitative analysis of the present data.

In order to rigorously test the effect of the M-H distance and Ni site symmetry on the observed Fe and Ni VtC spectra, we have performed a series of calculations in which the hydride is moved ± 0.4 Å from its equilibrium position in both **2** and **2*** towards either the Fe or the Ni center (Scheme 4). Hence, these calculations span Fe-H distances of **2** from 1.34 Å to 1.94 Å and 1.36 Å to 1.96 Å for **2***, respectively.

Starting from the optimized structure of **2** and allowing for the M-H bond to systematically vary, one obtains the calculated spectra shown in Figures 11a and b. In Figure 11a, it is observed that when the Fe-H bond is shortest the feature at ~ 7107 eV is at its maximum, while as the Fe-H bond elongates, the intensity of this feature is minimized. These trends provide further validation that the origin of this spectral feature is due to an Fe-H interaction. In contrast, examination of the calculated Ni VtC XES spectra for the same series (Figure 11b) shows only modest changes, despite the large variation in Ni-H distance. This provides further support for the lack of any significant Ni-H bonding in **2**.

In contrast, examination of the analogous M-H distance scan for **2*** reveals that significant spectral changes occur at both the Ni and the Fe as a function of M-H bond lengths (Figures 11c and d). As discussed above, in **2*** the hydride is able to interact more equally with both Fe and Ni at the equilibrium geometry. Hence, the changes in the Fe spectra as a function of Fe-H distance are diminished due to the presence of a Ni-H bonding interaction. The contributions of the hydride are evident at ~ 8324 and ~ 8329.5 eV in the Ni XES VtC spectra of **2*** (Figure 11d).

As **2** contains a Fe-hydride bond, which manifests in a clear observable feature at ~ 7107 eV in the experimental Fe VtC XES data, the series of calculations shown in Figure 11a may also be utilized as an experimental means to assess the Fe-H bond length. Figure 12 shows a comparison of the experimental Fe VtC XES data to the calculations in which the Fe-H bond length is allowed to vary from 1.47 Å to 1.77 Å. The dotted line provides the sigma and 3 sigma ranges for the experimental uncertainties in intensities. While these data suggest that VtC XES can in certain cases reveal M-H distances within ± 0.15 Å, the combined contributions of local site symmetry require the validity of such interpretations to be treated with caution.

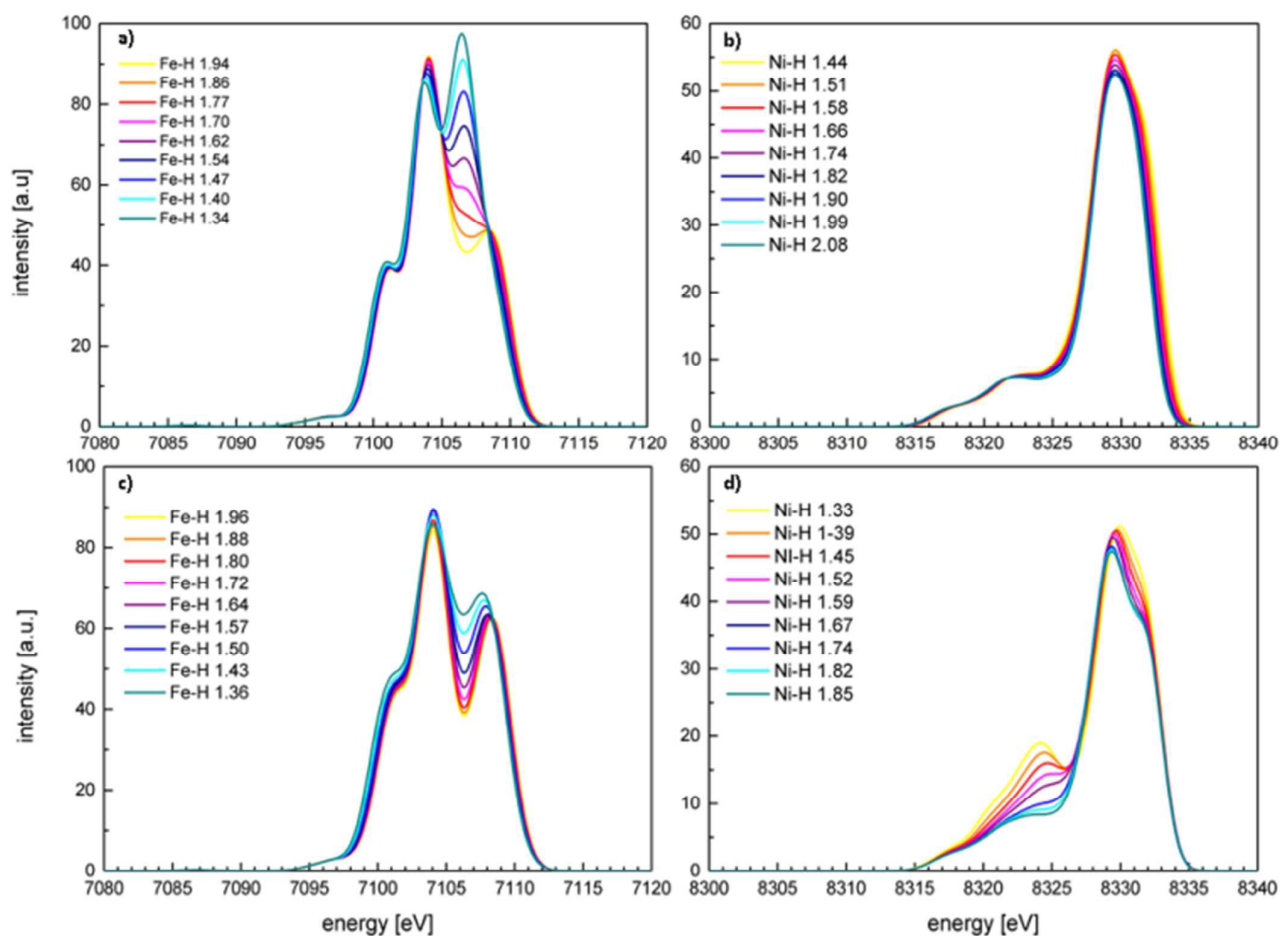


Figure 11 Figure 11 Metal-Hydride distance dependent calculated VtC XES spectra of **2** and **2***. a) Fe VtC XES of **2**; b) Ni VtC XES spectra of **2**; c) Fe VtC XES spectra of **2*** and d) Ni VtC XES spectra of **2***.

5. Conclusion

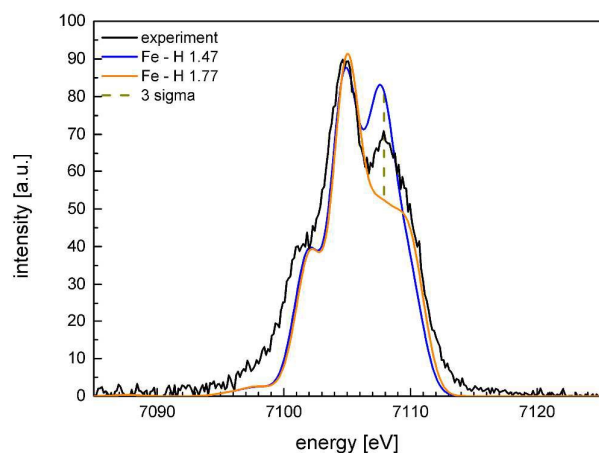


Figure 12 Comparison of calculated bond length to the experiment. VtC XES as a measure of metal-hydride distances gives a bond length between 1.47 and 1.77 Å.

In this work, the XAS and XES spectra of two NiFe hydrogenase model complexes (**1** and **2**) have been reported and the sensitivity

spectra show no direct contributions due to M-H interactions, and of the X-ray spectra to M-H interactions has been quantitatively assessed.

It has been demonstrated in the metal K-edge XAS that only secondary effects due to geometric distortions are observable. By contrast, the VtC XES spectra were shown to be sensitive to both the presence of M-H bonds and to geometric distortions at the absorbing atom. Through a detailed computational study, the effects of a change in local site symmetry and protonation of the metal center have been addressed in a stepwise fashion.

It is shown that **2** contains a true Fe-H bonding interaction, while the weaker Ni-H bond makes no significant contribution to the electronic structure. By distorting **2** to a hypothetical structure **2*** which no longer has a planar NiL₄ ligand environment (as in the [NiFe] hydrogenase enzyme), we show that both Fe-H and Ni-H bonding interactions are present. The lack of a Ni-H bond in **2** results from the local square planar symmetry of the NiL₄ unit, which raises the energy of the d_{x²-y²} orbital and makes the formation of an Ni-H bond unfavorable. It thus appears that the ability of the protein to maintain a local non-planar NiL₄ geometry may be a key feature in optimizing the reactivity of the enzymatic

active site. In fact, recent studies by Rauchfuss and coworkers resulted in a closely related hypothesis³². These results provide motivation for the synthesis of model complexes in which a non-planar NiL₄ symmetry at the Ni is enforced.

In addition, the ability to use VtC XES as an experimental means to assess M-H bond lengths has been investigated. While the uncertainties are relatively large (± 0.15 Å), when viewed together with other spectroscopic data, VtC XES may provide additional experimental evidence for the presence and strength of M-H interactions.

Finally, we note that the present study emphasizes the enhanced information content, which can be achieved by performing XES measurements at two different metal absorbers. Experimental setups which would enable the changes that occur at both the Ni and the Fe centers to be followed simultaneously are presently being developed at synchrotrons facilities and free electron lasers.⁶⁷

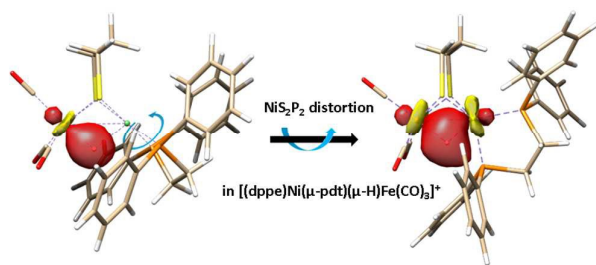
Acknowledgements

Financial support granted by the Max-Planck-Society is gratefully acknowledged. H. S. Shafaat acknowledges a Postdoctoral Research Fellowship from the Alexander von Humboldt Foundation. Use of the Stanford Synchrotron Radiation Lightsource, SLAC National Accelerator Laboratory, is supported by the U.S. Department of Energy, Office of Science, Office of Basic Energy Sciences under Contract No. DE-AC02-76SF00515.

References

- 1 V. Artero, G. Berggren, M. Atta, G. Caserta, S. Roy, L. Pecqueur, M. Fontecave, *Acc. Chem. Res.*, 2015, **48**, 2380-2387.
- 2 H. S. Shafaat, O. Rüdiger, H. Ogata, W. Lubitz, *Biochim. Biophys. Acta*, 2013, **1827**, 986-1002.
- 3 W. Lubitz, E. Reijerse, M. v. Gastel, *Chem. Rev.*, 2007, **107**, 4331-4365.
- 4 W. Lubitz, H. Ogata, O. Rüdiger, E. Reijerse, *Chem. Rev.*, 2014, **114**, 4081-4148.
- 5 E. Kempainen, A. Bodin, B. Sebok, T. Pedersen, B. Seger, B. Mei, D. Bae, P. C. K. Vesborg, J. Halme, O. Hansen, P. D. Lund, I. Chorkendorff, *Energy Environ. Sci.*, 2015, **8**, 2991-2999.
- 6 Liu, X., Ibrahim, S. K., Tard, C., Pickett, C. J., *Coord. Chem. Rev.*, 2005, **249**, 1641-1652.
- 7 Capon, J.-F., Gloaguen, F., Schollhammer, P., Talarmin, J. *Coord. Chem. Rev.*, 2005, **249**, 1664-1676.
- 8 G. A. N. Felton, C. A. Mebi, B. J. Petro, A. K. Vannucci, D. H. Evans, R. S. Glass, D. L. Lichtenberger, *J. Organomet. Chem.*, 2009, **694**, 2681-2699.
- 9 A. Kochem, E. Bill, F. Neese, M. van Gastel, *Chem. Commun.*, 2015, **51**, 2099-2102.
- 10 B. J. Murphy, R. Hidalgo, M. M. Roessler, R. M. Evans, P. A. Ash, W. K. Myers, K. A. Vincent, F. A. Armstrong, *J. Am. Chem. Soc.*, 2015, **137**, 8484-8489.
- 11 S. Canaguier, M. Field, Y. Oudart, J. Pécaut, M. Fontecave, V. Artero, *Chem. Commun.*, 2010, **46**, 5876-5878.
- 12 B. L. Greene, C. - H. Wu, P. M. McTernan, M. W. W. Adams, R. B. Dyer, *J. Am. Chem. Soc.*, 2015, **137**, 4558-4566.
- 13 A. Dutta, G. A. Hamilton, H. E. Hartnett, A. K. Jones, *Inorg. Chem.*, 2012, **51**, 9580-9588.
- 14 H. S. Shafaat, K. Weber, T. Petrenko, F. Neese, W. Lubitz, *Inorg. Chem.*, 2012, **51**, 11787-11797.
- 15 T. R. Simmons, V. Artero, *Angew. Chem. Int. Ed.*, 2013, **52**, 6143-6145.
- 16 G. M. Chambers, M. T. Huynh, Y. Li, S. Hammes-Schiffer, T. B. Rauchfuss, E. Reijerse, W. Lubitz, *Inorg. Chem.*, 2015, DOI: 10.1021/acs.inorgchem.5b01662.
- 17 Z. Li, Y. Ohki, K. Tatsumi, *J. Am. Chem. Soc.*, 2005, **127**, 8950-8951.
- 18 T. Burgdorf, O. Lenz, T. Buhrke, E. v.d.Linden, A. Jones, S. Albracht, B. Friedrich, *J. Mol. Microbiol. Biotechnol.*, 2005, **10**, 181-196.
- 19 P. Wulff, C. C. Day, F. Sargent, F. A. Armstrong, *PNAS*, 2014, **111**, 6606-6611.
- 20 W. Lubitz, E. Reijerse, M. v.Gastel, *Chem. Rev.*, 2007, **107**, 4331-4365.
- 21 A. L. De Lacey V. M. Fernández, M. Rousset, R. Cammack, *Chem. Rev.*, 2007, **107**, 4304-4330.
- 22 M. Brecht, M. v. Gastel, T. Buhrke, B. Friedrich, W. Lubitz, *J. Am. Chem. Soc.*, 2003, **125**, 13075-13083.
- 23 H. Ogata, K. Nishikawa, W. Lubitz, *Nature*, 2015, **520**, 571-574.
- 24 H. Ogata, T. Krämer, H. Wang, D. Schilter, V. Pelmenshikov, M. v. Gastel, F. Neese, T. B. Rauchfuss, L. B. Gee, A. D. Scott, Y. Yoda, Y. Tanaka, W. Lubitz, S. P. Cramer, *Nature Comm.*, 2015, **6**, 7890.
- 25 W. Zhu, A. C. Marr, Q. Wang, F. Neese, D. J. E. Spencer, A. J. Blake, P. A. Cooke, C. Wilson, M. Schröder, *PNAS*, 2005, **102**, 18280-18285.
- 26 B. E. Barton, C. M. Whaley, T. B. Rauchfuss, D. L. Gray, *J. Am. Chem. Soc.*, 2009, **131**, 6942-6943.
- 27 B. E. Barton, T. B. Rauchfuss, *J. Am. Chem. Soc.*, 2010, **132**, 14877-14885.
- 28 M. E. Carroll, B. E. Barton, D. L. Gray, A. E. Mack, T. B. Rauchfuss, *Inorg. Chem.*, 2011, **50**, 9554-9563.
- 29 K. Weber, T. Krämer, Hannah, S. Shafaat, T. Weyhermüller, E. Bill, M. v. Gastel, F. Neese, W. Lubitz, *J. Am. Chem. Soc.*, 2012, **134**, 20745-20755.
- 30 S. Ogo, K. Ichikawa, T. Kishima, T. Matsumoto, H. Nakai, K. Kusaka, T. Ohhara, *Science*, 2013, **339**, 682-684.
- 31 M. v. Gastel, M. Stein, M. Brecht, O. Schröder, F. Lenzian, R. Bittl, H. Ogata, Y. Higuchi, W. Lubitz, *J. Biol. Inorg. Chem.*, 2006, **11**, 41-51.

- 32 M. T. Huynh, D. Schilter, S. Hammes-Schiffer, T. B. Rauchfuss, *J. Am. Chem. Soc.*, 2014, **136**, 12385-12395.
- 33 C. J. Pollock, M. U. Delgado-Jaime, M. Atanasov, F. Neese, S. DeBeer, *J. Am. Chem. Soc.*, 2014, **136**, 9453-9463.
- 34 M. U. Delgado-Jaime, B. R. Dible, K. P. Chiang, W. W. Brennessel, U. Bergmann, P. L. Holland, S. DeBeer, *Inorg. Chem.*, 2011, **50**, 10709-10717.
- 35 K. M. Lancaster, M. Roemelt, P. Ettenhuber, Y. Hu, M. W. Ribbe, F. Neese, U. Bergmann, S. DeBeer, *Science*, 2011, **334**, 974-977.
- 36 Y. Pushkar, X. Long, P. Glatzel, G. W. Brudvig, G. C. Dismukes, T. J. Collins, V. K. Yachandra, J. Yano, U. Bergmann, *Angew. Chem. Int. Ed.*, 2010, **49**, 800-803.
- 37 C. Lambertz, P. Chernev, K. Klingan, N. Leidel, K. G. V. Sigfridsson, T. Happe, M. Haumann, *Chem. Sci.*, 2014, **5**, 1187-1203.
- 38 M. U. Delgado-Jaime, S. DeBeer, M. Bauer, *Chem. Euro. J.*, 2013, **19**, 15888-15897.
- 39 M. U. Delgado-Jaime, P. Kennepohl, *J. Synch. Rad.*, 2009, **17**, 119-128.
- 40 M. U. Delgado-Jaime, C. P. Mewis, P. Kennepohl, *J. Synch. Rad.*, 2009, **17**, 132-137.
- 41 F. Neese, ORCA, version 3.0, Max Planck Institute for Chemical Energy Conversion: Mülheim/Ruhr, Germany, 2014
- 42 A. D. Becke, *Phys. Rev. A*, 1988, **38**, 3098-3100.
- 43 J. P. Perdew, *Phys. Rev. B*, 1986, **33**, 8822-8824.
- 44 E. J. Baerends, D. E. Ellis, P. Ros, *Chem. Phys.*, 1973, **2**, 41-51.
- 45 B. I. Dunlap, J. W. D. Connolly, J. R. Sabin, *J. Chem. Phys.*, 1979, **71**, 3396-3402.
- 46 O. Vahtras, J. Almlöf and M. W. Feyereisen, *Chem. Phys. Lett.*, 1993, **213**, 514-518.
- 47 F. Neese, *J. Comp. Chem.*, 2003, **24**, 1740-1747.
- 48 D. A. Pantazis, X. Y. Chen, C. R. Landis, F. Neese, *J. Chem. Theory Comp.*, 2008, **4**, 908-919.
- 49 F. Weigend, *Phys. Chem. Chem. Phys.*, 2006, **8**, 1057-1065.
- 50 K. Eichkorn, O. Treutler, H. Ohm, M. Haser, R. Ahlrichs, *Chem. Phys. Lett.*, 1995, **240**, 283-289.
- 51 K. Eichkorn, F. Weigend, O. Treutler, R. Ahlrichs, *Theo. Chem. Acc.*, 1997, **97**, 119-124.
- 52 F. Neese, *Inorg. Chim. Acta*, 2002, **337**, 181-192.
- 53 A. Klamt, G. Schüürmann, *J. Chem. Soc. Perkin. Trans.*, 1993, **2**, 799-805.
- 54 S. DeBeer George, T. Petrenko, F. Neese, *J. Phys. Chem. A*, 2008, **112**, 12936-12943.
- 55 S. DeBeer George, T. Petrenko, F. Neese, *Inorg. Chim. Acta*, 2008, **361**, 965-972.
- 56 N. Lee, T. Petrenko, U. Bergmann, F. Neese, S. DeBeer, *J. Am. Chem. Soc.*, 2010, **132**, 9715-9727.
- 57 M. U. Delgado-Jaime, S. DeBeer, *J. Comp. Chem.*, 2012, **33**, 2180-2185.
- 58 T. E. Westre, P. Kennepohl, J. G. DeWitt, B. Hedman, K. O. Hodgson, E. J. Solomon, *J. Am. Chem. Soc.*, 1997, **119**, 6297-6314.
- 59 S. C. Stieber, C. Milsmann, J. M. Hoyt, Z. R. Turner, K. D. Finkelstein, K. Wieghardt, S. DeBeer, P. J. Chirik, *Inorg. Chem.*, 2012, **51**, 3770-3785.
- 60 M. U. Delgado-Jaime, B. R. Dible, K. P. Chiang, W. W. Brennessel, U. Bergmann, P. L. Holland, S. DeBeer, *Inorg. Chem.*, 2011, **50**, 10709-10717.
- 61 Z. Gu, J. Dong, C. B. Allan, S. B. Choudhury, R. Franco, J. H. G. Moura, I. Moura, J. LeGall, A. Przybyla, W. Roseboom, S. P. J. Albracht, M. J. Axley, R. A. Scott, M. M. Marony, *J. Am. Chem. Soc.*, 1996, **118**, 11155-11165.
- 62 M. Roemelt, M. A. Beckwith, C. Duboc, M. - N. Collomb, F. Neese, S. DeBeer, *Inorg. Chem.*, 2012, **51**, 680-687.
- 63 V. Krewald, B. Lassalle-Kaiser, T. T. Boron III, C. J. Pollock, J. Kern, M. A. Beckwith, V. K. Yachandra, V. L. Pecoraro, J. Yuno, F. Neese, S. DeBeer, *Inorg. Chem.*, 2013, **52**, 12904-12914.
- 64 R. H. Summerville, R. Hoffmann, *J. Am. Chem. Soc.*, 1976, **98:23**, 7240-7254.
- 65 C. J. Pollock, K. Grubel, P. L. Holland, S. DeBeer, *J. Am. Chem. Soc.*, 2013, **135**, 11803-11808.
- 66 U. Bergmann, C. R. Horne, T. J. Collins, J. M. Workman, S. P. Cramer, *Chem. Phys. Lett.*, 1999, **302**, 119-124.
- 67 S. Gul, J. W. Desmond Ng, R. Alonso-Mori, J. Kern, D. Sokaras, E. Anzenberg, B. Lassalle-Kaiser, Y. Gorlin, T.-C. Weng, P. H. Zwart, J. Z. Zhang, U. Bergmann, V. K. Yachandra, T. F. Jaramillo, J. Yano, *Phys. Chem. Chem. Phys.*, 2015, **17**, 8901-8912.



Insight into the factors that favor metal-hydride interactions in NiFe-hydrogenase models is obtained through X-ray spectroscopic and quantum chemical studies.